Surface roughness parameter and modeling for fatigue behavior of additive manufactured parts: A non-destructive data-driven approach

Seungjong Lee [a,b], Behnam Rasoolian [c], Daniel F. Silva [b,c], Jonathan W. Pegues [d], Nima Shamsaei [a,b,*]

[a] Department of Mechanical Engineering, Auburn University, Auburn, AL 36849, USA
[b] National Center for Additive Manufacturing Excellence (NCAME), Auburn University, Auburn, AL 36849, USA
[c] Department of Industrial and Systems Engineering, Auburn University, Auburn, AL 36849, USA
[d] Material, Physical, and Chemical Sciences Center, Sandia National Laboratories, Albuquerque, NM 87185, USA

ARTICLE INFO

ABSTRACT

Metallic additive manufacturing produces undesired surface roughness due to the nature of the layer-by-layer fabrication process. As-built surface roughness can accelerate surface crack initiation and result in an early fatigue failure under cyclic loading. Therefore, the effect of surface roughness on the structural integrity of additive manufactured parts needs to be characterized before they can be used in fatigue-critical applications. In this study, the surface roughness of Ti-6Al-4V specimens fabricated by a laser beam powder bed fusion system is characterized, using a non-destructive data-driven approach, and correlated with their fatigue performance. Using a data-intensive surface topographical investigation, standard surface roughness parameters with statistical robustness are generated. The results confirm that conventional standard surface roughness parameters cannot appropriately represent the correlation between surface roughness and fatigue lives. Accordingly, a hybrid surface roughness parameter consisting of the maximum valley depth (R_v/S_v), the skewness (R_{sk}/S_{sk}), and the kurtosis (R_{ku}/S_{ku}) of the profiled lines/areas is suggested to explain the fatigue behavior. The proposed hybrid surface roughness parameter is validated by vertically fabricated flat specimens and diagonally built cylindrical dog-bone specimens to investigate the effect of design and build orientation. Moreover, a fatigue prediction model which considers the surface roughness as a micro-notch has been modified using the proposed hybrid surface roughness parameter and the part's layer thickness and validated against experimental data.

1. Introduction

The advancement of metallic additive manufacturing (AM) has enabled the fabrication of complex geometries that are otherwise unobtainable through traditional subtractive methods. Among the various metallic additive manufacturing methods, laser beam powder bed fusion (LB-PBF) has gained more attention because it can fabricate components with high resolution compare to other AM processes, which is partially due to utilizing smaller size of powder particles and thinner layer thickness [1–4]. Therefore, the biomedical and aerospace industries have shown particular interest in LB-PBF for fabrications that require meticulous and complex geometries such as bone implants and lattice structures [2,3,5]. While significant research works have been conducted to investigate many different aspects such as mechanical and material behaviors of parts fabricated via LB-PBF [6–10], a comprehensive understanding of the effect of surface roughness on fatigue behavior is not yet fully obtained.

Titanium alloys are commonly-used materials for biomedical and aerospace applications because of their remarkable properties such as high strength to weight ratio, corrosion resistance, and weldability [11, 12]. Among the various titanium alloys, Ti-6Al-4V, composed of hexagonal close-packed alpha-phase and body-centered cubic beta phase, is the most widely used [12,13]. Therefore, Ti-6Al-4V has been studied by many researchers and adapted by the AM community to utilize in several applications [14–16]. LB-PBF Ti-6Al-4V, especially, has been investigated in terms of microstructural and mechanical characterization to understand the process-structure-property relationships specific to this

AM process [14,17–19]. Accordingly, appropriate processing methods and process parameters have been suggested to reliably fabricate LB-PBF Ti-6Al-4V components that have comparable static properties to conventionally manufactured counterparts [20,21].

Among the various mechanical properties, however, LB-PBF Ti-6Al-4V parts show relatively inferior fatigue strength compared to conventionally manufactured counterparts [22,23]. One of the main demands for additively manufactured (AM) components is for fatigue critical applications, hence comprehending the fatigue behavior of AM parts is very important [22–24]. LB-PBF process produces unavoidable internal defects such as gas entrapped pores and lack-of-fusion defects which notably deteriorate the fatigue strength compared to microstructural effects. In order to enhance the fatigue performance of LB-PBF Ti-6Al-4V, multiple studies have been conducted in terms of optimizing process parameters and performing various post-process treatments such as conventional heat-treatment, hot isostatic pressing, and various surface enhancement techniques [17,25,26]. Improved fatigue lives can be obtained through these post-process treatments, with the most beneficial effect on fatigue behavior being obtained by subtractive machining processes to remove the as-built surfaces [27].

The surface roughness (SR) in AM parts is inevitable due to the layer-by-layer fabrication process as well as the attachment of partially melted powder particles to the surface [3,8,28]. SR is deleterious to the fatigue performance, even though LB-PBF fabricates components with relatively low SR compared to other AM techniques, such as direct energy deposition [29–33]. Various surface enhancement techniques such as machining, shot-peening, and laser polishing have been proposed to reduce the SR and result in an improved fatigue performance [34–39]. However, besides the cost and time associated with these surface enhancement techniques, such treatments are difficult to conduct on complex geometries such as porous/lattice components or parts with internal features. Therefore, utilizing AM parts without the need of extensive surface enhancement is an outstanding goal in the AM community. An overall understanding of SR effects on fatigue resistance of AM parts and establishing predictive methods are required to accomplish this goal.

The standard SR terminology was developed by the International Organization of Standardization (ISO) [40], and those standardized SR parameters are widely used in the conventional manufacturing community as well as in the AM community [28,41]. Among the various standard SR parameters, the arithmetical mean height (R_a for line and S_a for area roughness) which indicates the average of the height along the profiled region is most commonly used since it can describe the general topography of a surface [42]. SR induced fatigue failures, however, are dependent on localized crack initiations due to plastic deformations corresponding to stress concentrations at the critical micro-notches. As a result, the maximum profile valley depth (R_v for line and S_v for area roughness) which indicates the lowest point from the mean line is usually used for fatigue analysis [43].

Furthermore, calculating the stress concentration factor which introduces early fatigue life crack initiation requires both the depth of SR and the topographical factors such as radii and steepness of valleys [44,45]. Some works have suggested estimating fatigue lives based on the combination of standard SR parameters and the radii of ten deepest valleys on the surface [46,47]. The proposed models, however, involve constraints; limited precision of techniques for characterizing surface topography to identify the radii, the human induced artificial inaccuracy of estimating radii from the obtained data, and more. The measurement of surface features (e.g. radii of ten deepest valleys) especially may cause disparities between observers due to the lack of standard criteria for determining these dimensions. Therefore, a simplified model using modified hybrid SR parameter seems to be critical to understand and estimate the fatigue behavior without introducing unnecessary errors.

In this study, the SR for LB-PBF Ti-6Al-4V specimens in as-built and half-polished surface conditions have been thoroughly characterized by empirical analysis using digital microscopy. Not only the numerical standard SR parameters, but also the alteration of radii and steepness of surface notches are considered before and after the polishing process. In addition, hybrid area SR parameters including the maximum valley depth of the profiled surface (S_v), the distance between the mean and the most frequently observed value of the profiled surface (S_{mode}), the kurtosis of the profiled surface (S_{ku}), and the skewness of the profiled surface (S_{sk}) are calculated. Subsequently, the specimens with various surface conditions have been tested under cyclic loading. The correlation of various SR parameters with fatigue lives of as-built and half-polished specimens, especially in the high cycle fatigue (HCF) regime, is examined. In addition, the hybrid line SR parameter as a substitute for the hybrid area SR parameter is investigated to be utilized for parts with complex geometries that do not allow measuring the surface easily. Finally, a proposed hybrid line SR parameter is employed to predict fatigue performance and the results are compared with experimental data.

2. Material and methods

2.1. Experimental procedures

A net shape flat specimen with a uniform rectangular gage section was designed for this study based on ASTM E466 [48], as shown in Fig. 1. Grade 23 alpha-beta Ti-6Al-4V powder made by Carpenter Additive was used to fabricate specimens. The chemical composition of the powder is listed in Table 1. The specimens were fabricated by an EOS M290 LB-PBF machine using the default process parameters for Ti-6Al-4V as follows: laser power of 280 W, laser scan speed of 1200 mm/s, hatching distance of 0.14 mm, and layer thickness of 30 μm. The build orientation was vertical and the entire build process was conducted under argon atmosphere. Before detaching specimens from the substrate, the whole plate was stress relieved under an argon
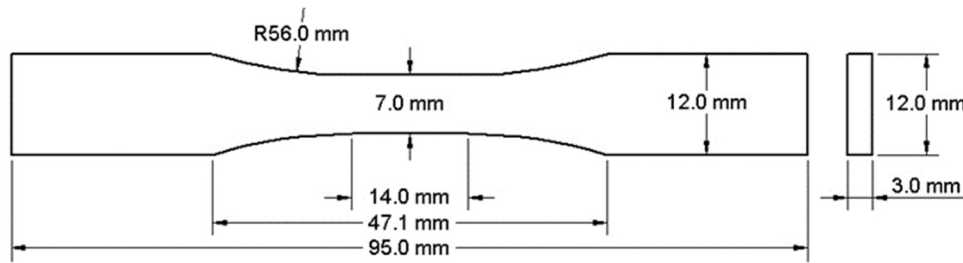
Fig. 1. The design and dimensions of fatigue specimens based on ASTM E466 [48], the standard test method for force-controlled fatigue testing.

Table 1
The chemical composition of Ti-6Al-4V powder produced by Carpenter Additive.

Element	Al	C	Fe	H	N	O	Ti	V
wt%	6.2	0.01	0.09	0.002	0.01	0.09	Bal	4.0

environment at 700 ℃ for an hour and furnace cooled to eliminate the effect of residual stresses [49,50]. After stress relief, the specimens were carefully removed from the substrate to preserve the as-built surfaces.

Two categories of surface conditions, as-built and half-polished, were investigated in this study to explore the effect of peaks and valleys on fatigue behavior. The goal of the half-polished condition is to isolate the effects of the valleys and identify the role, if any, the peaks may have on the fatigue resistance. For the half-polished surface condition, the specimens were manually hand-polished, using abrasive papers with a grit size of 320, enough to eliminate the relatively higher peaks on the surface while not affecting the valleys. According to the caliper measurement, the thickness of half-polished specimens was decreased by approximately 0.1 mm. In addition, the sides of the specimens were mirror-polished (less than 0.2 µm SR based on ASTM E466 [48]) in order to prevent crack initiations from the side surfaces. The surface topography of the gage section of as-built and half-polished specimens was measured using a Keyence VHX-6000 3D digital microscope. Every specimen (18 in total, 9 of each as-built and half-polished condition) was investigated to obtain more raw data that provide enough sample size for statistical analysis. The obtained 3D surface images were converted to.csv point height data to facilitate further surface topographical data investigation.

Strain- followed by force-controlled uniaxial fatigue tests with strain/stress ratio of $R_\varepsilon = 0.1$ and $R_\sigma = 0.1$ were conducted on an MTS Landmark servo-hydraulic test frame with a load capacity of 100 kN. The switch to pseudostrain control under force control once cyclic stability is achieved provides flexibility for testing in the HCF regime and was considered in this study following note 5 in ASTM E606 [51]. The strain/stress ratio was set to 0.1 to prevent buckling failures. According to Pegues et al. [32], SR should be excluded from the load-bearing areas calculated by manually measured cross-sections. Therefore, the strain-controlled tests were conducted first up to ~200 cycles by the extensometer attached on the side of the specimen to obtain the constitutive stress-strain relationship for each test. The control mode was then switched to force-control based on the obtained force from the strain-controlled portion of the test and progressed up until failure. If the running cycles reached 5 million cycles (10 million reversals), the test was suspended and considered as run-out. Ti-6Al-4V specimens show mostly linear hysteresis loops and very stable cyclic behavior without cyclic hardening or softening so the tests can be simply regarded as force-controlled tests.

The fractography analysis was performed on the final fracture surfaces to find crack initiation cites from the as-built and half-polished surface regions. The overall fracture surfaces were observed by Keyence VHX-6000X using 3D stitching mode to cover the entire area. Contour maps of final fracture surfaces were generated using the obtained point height data to investigate the crack initiation regions.

2.2. Data pre-processing

The images obtained from the 3D digital microscope were converted from.csv format to a binary format. A pixel in a 500X microscopy image represents approximately a 0.429×0.429 µm surface area. Therefore, each file contains about $15,000 \times 15,000$ data points. The images were appropriately down-sampled to reduce the computational expense so each pixel represents 1×1 µm area. Further smoothing was done by applying a 2D Gaussian kernel of size 5×5 and a standard deviation of 1 to the images. Slight smoothing is necessary to remove ridges that might be caused by digital noise.

It was observed that the specimens were not aligned exactly parallel to the image frame. Such misalignments were programmatically detected and fixed since they can potentially have a significant influence on the calculation of standard SR parameters. Fig. 2 describes how misalignments were corrected with (a) reconstructed and (b) schematic surface images. The alignment adjustment was performed by fitting a line to the upper edge of the specimen in the image using linear regression. The upper edge is detected via adaptive thresholding which separates the specimen from the background. A rotation angle can be extracted from the slope of the fitted line. Finally, the image is rotated by this angle in the opposite direction, resulting in an upper edge with angle 0°.

In addition, as an artifact of the microscopy process, the surface of the parts may not be perfectly flat when the images are obtained. For example, it might be slightly tilted from one side to the other as illustrated in Fig. 3(a) and (b) as 3D and 2D demonstrations, respectively. These tilts were also programmatically detected and corrected. The procedure of tilt adjustment is performed by regressing a 2D plane to the surface of the image in the form of:

$$aX + bY = Z \tag{1}$$

where X and Y are pixel coordinates and Z is the intensity of the pixel in the image. The parameters a and b are estimated by a regression that fits a plane to the surface of the image. Finally, a correction is made on the intensities subtracting estimated intensity from the actual intensity of each pixel:

$$Z' = Z - (aX + bY) \tag{2}$$

where Z′ is the zero-centered and corrected surface height after tilt adjustment.

The top and bottom images of Fig. 3(a) illustrate the same location with original and tilt-adjusted views. Note how the coloring of minima and maxima changes before and after tilt adjustment. To verify the alternation of height numerically, 2D profiles of surfaces in Fig. 3(a) were generated as shown in Fig. 3(b). This figure illustrates the average pixel intensities over the x-axis in the image before and after tilting. Note how the intensity profile is flattened in Fig. 3(b) after the process. In this study, all height data acquired from images passed through the above steps to adjust the alignment and tilt of the images, to minimize numerical errors in further SR analysis.
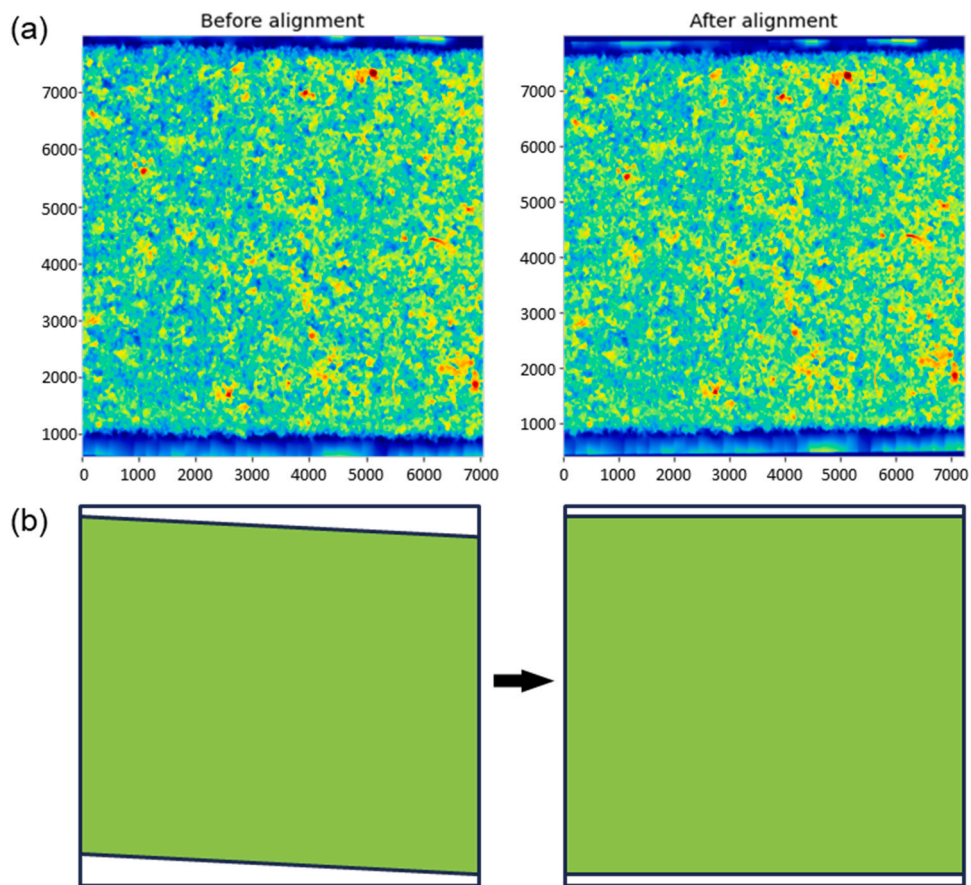
Fig. 2. The descriptions of before and after the misalignment correction using (a) reconstructed and (b) schematically drawn surface images. The units are μm.
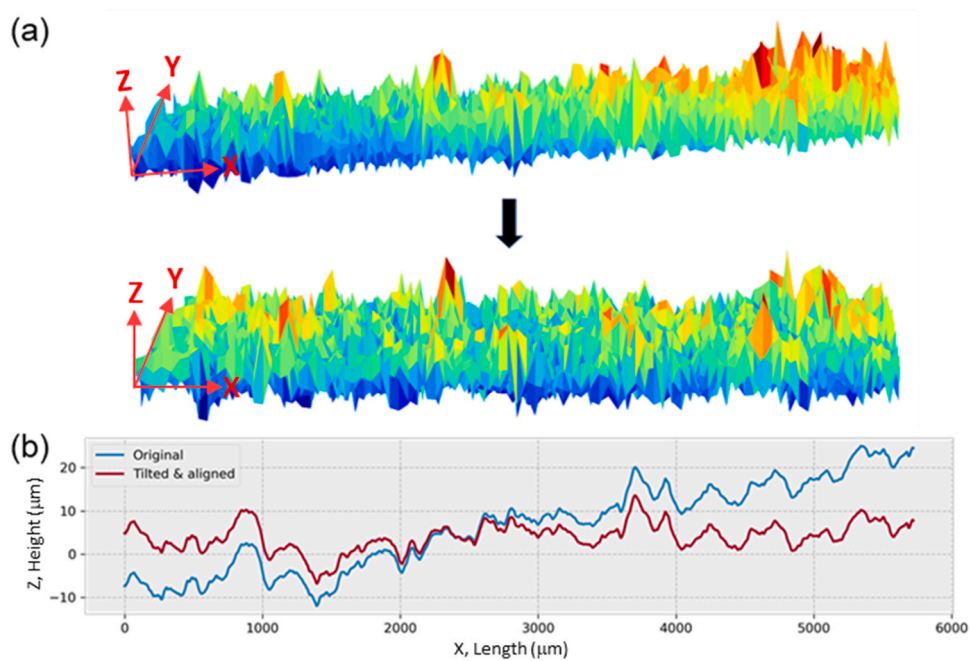

Fig. 3. (a) 3D demonstration of tilt correction and (b) 2D profiled lines before and after tilt/alignment correction with numerical height values.

3. Experimental results

3.1. Surface topography

One challenge faced when comparing images before and after polishing, is matching the as-built microscopy image to the one obtained after polishing. Fig. 4 shows the surface topography of a specimen using a color map that indicates peaks in red and valleys in blue: (a) before polishing (as-built) and (b) after polishing (half-polished). Most of the peaks from the as-built surface (Fig. 4(a)) were removed in the polishing process which resulted in relatively lower and flatter peaks as shown in the half-polished part (Fig. 4(b)). Interestingly, a valley observed in the half-polished surface (black dotted circle Fig. 4(b)) used to be a peak in the as-built surface (black dotted circle Fig. 4(a)). The results show the presence of "hidden" valleys underneath peaks, which may be caused by partially melted features on the surface, using the comparison between as-built and half-polished surface topographies. The "hidden" valleys were also claimed from other studies using images of the polished transverse sections close to the surface of specimens [52]. Therefore, surface topography via optical methods may not exactly pinpoint local minima that can initiate fatigue cracks due to the possible presence of deep/sharp valleys that are occluded from the view of microscope by unmelted powder resting on the surface.

The conventional standard SR parameters based on the ISO 4287:1997 [40] are calculated and listed in Table 2, including both one-dimensional line roughness and two-dimensional area roughness. Linear (1D) metrics are averages taken over all the line profiles in the image. According to Table 2, all values that indicate height of profiled
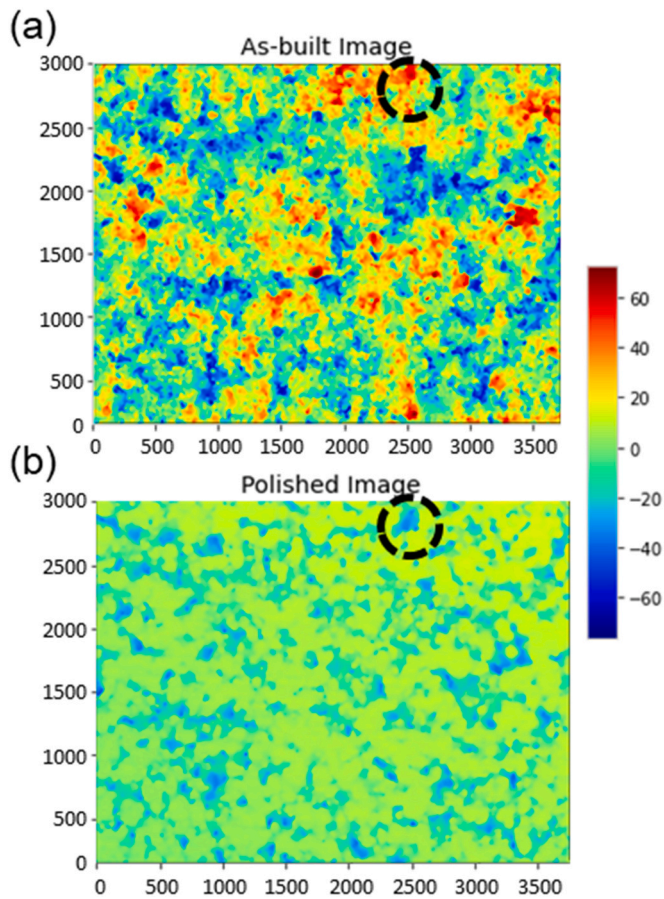

Fig. 4. Reconstructed surface topography of a specimen (a) before and (b) after half-polishing from the top view using Python. Black dotted circles indicate "hidden" valleys which were not distinguished before polishing. All units are μm.

Standard SR parameters	As-built		Half-polished	
	1D (line)	2D (area)	1D (line)	2D (area)
Arithmetical mean height (R_a/S_a)	18.8 μm	19.8 μm	9.0 μm	11.6 μm
Root mean square deviation (R_q/S_q)	23.2 μm	24.5 μm	11.0 μm	14.0 μm
Maximum profile peak height (R_p/S_p)	62.8 μm	111.8 μm	15.5 μm	31.0 μm
Maximum profile valley depth (R_v/S_v)	58.7 μm	87.7 μm	35.2 μm	56.7 μm
Kurtosis (R_{ku}/S_{ku})	2.9	2.9	3.9	2.7
Skewness (R_{sk}/S_{sk})	0.1	0.1	−1.0	-0.6
Distance between the mean and mode (R_{mode}/S_{mode})	−0.8 μm	−3.1 μm	8.2 μm	9.5 μm

line/surface such as R_a/S_a, R_q/S_q, R_p/S_p, and R_v/S_v were decreased after polishing. Even though the surface was half-polished, R_v and S_v were also decreased. This is due the fact that R_v and S_v are calculated based on distances from the mean and the mean goes down when peaks are flattened through polishing. This observation confirmed that simple standard SR height parameters (such as R_v/S_v) can be skewed due to the effect of the average characteristics of the surface height, which do not affect the mechanical performance.

To explore the effect of polishing on height data distribution, surface topography was investigated by comparing profiles from the same region of a specimen in three different polishing states: as-built, polished and more polished. Fig. 5 shows profile lines for the three different polishing states in (a) and their height probability density in (b). A profile which does not cross the aforementioned "hidden" valleys and can cause undesirable differences in height distribution was selected. As shown in Fig. 5(a), the peaks of the surface were flattened by the light hand-polishing processes and indicated as dotted lines with corresponded colors for each condition. It should be noted that these dotted lines illustrate how much depth of material has been removed and they are matched with the highest height probability density as shown in Fig. 5(b). On the other hand, the valleys, and their topographical features such as radii of valleys indicated by blue shaded areas in Fig. 4 were not significantly affected by the polishing processes.

The height distribution indicated by height probability density in Fig. 5(b) can be examined using skewness, kurtosis, and the location of modes. Skewness is a measure of asymmetry of the distribution. A completely symmetric distribution has a skewness of zero and asymmetric distributions have either negative or positive skewness depending on the location of peaks. Kurtosis is a measure of weight of the tails of the distribution. A high kurtosis means there is a higher probability for extreme values to occur. The as-built surface had a height distribution with a lower kurtosis (resulting in a wide distribution) and a skewness close to zero (resulting in a less distance between the mean and median). On the other hand, the height distribution of polished surfaces shows a relatively higher kurtosis and a negative skewness, indicating that the height data has asymmetry and more extreme values correlated to the valleys, which are more influential to fatigue resistance. Tracking the changes in peaks show that as the process of polishing continues, the top peaks are reduced proportional to the amount of polishing. This can be explained by the fact that polishing flattens the peaks, resulting in a larger number of high points with roughly the same height. This observation verifies that surface polishing can influence the characteristics of the height data distribution, while not eliminating the deleterious effect of the valleys on fatigue performance. Therefore, some of the standard SR parameters cannot adequately characterize the influence of surface condition on fatigue resistance.
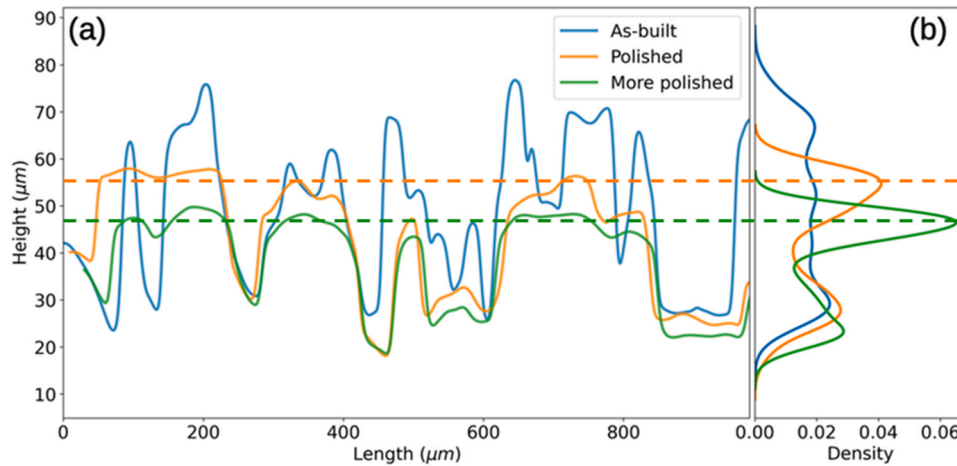
Fig. 5. (a) 1D surface topography and (b) height probability density of the profiles along with the build orientation and loading direction of as-built, half-polished, and more-polished surfaces.

3.2. Fatigue and fractography

The strain- followed by force-controlled fatigue testing results are listed in Table 3, including frequency, applied maximum strain (ε_{max}), applied minimum strain (ε_{min}), strain ratio (R_ε), maximum stress response (σ_{max}), minimum stress response (σ_{min}), stress ratio (R_σ) and reversals to failure ($2N_f$). The effective cross sectional area is calculated by offsetting the total height of profiled surface (S_t) to obtain the applied maximum stresses by only considering the load-bearing area. Based on the data points in Table 3, the strain-life and stress-life fatigue plots are generated and presented in Fig. 6. The red squares and blue circles in Fig. 6 represent as-built and half-polished specimens, respectively. The run-out data points are indicated by arrows with each corresponding color. Under $\varepsilon_{max} = 0.0020$ mm/mm ($\sim \sigma_{max} = 445$ MPa), specimens with either surface condition reached 10^7 reversals, and therefore, are marked as run-outs.

As can be seen from Fig. 6, fatigue lives are very similar for both as-built and half-polished surface conditions among all cycle regimes. It has been shown that, depending on the ductility, the effect of SR on fatigue strength in low cycle fatigue (LCF) and intermediate cycle fatigue (ICF) regimes is not as significant due to the global plastic behavior leading to a much greater influence of the crack growth rather than crack initiation [47]. On the other hand, SR can be much more influential in the HCF regime since the fatigue failure in this life regime is mostly governed by the crack initiation process, which can be affected by the SR significantly

in the absence of plastic deformation. Therefore, the specimens with lower SR will generally have longer fatigue lives compared to the specimens with higher SR in the HCF regime. Interestingly, data points in the HCF regime ($\varepsilon_{max} = 0.0020$ and 0.0025 mm/mm) in this study indicate that as-built and half-polished specimens have similar fatigue lives even though their standard SR parameters are quite distinct. The standard SR parameters provided in Table 2 suggest that the negative impact of SR on fatigue performance would be reduced for the half-polished conditions. However, the similar fatigue performance observed for the two distinct surface conditions demonstrate the valleys, which provide the critical crack initiation features under cyclic loading, are not significantly altered, their detrimental effect on fatigue performance is not reduced. This is a cautionary example of the complexities associated with correlating fatigue properties to surface topography and the need for new parameters that are capable of distinguishing critical differences in surface conditions affecting fatigue.

According to the fractographic analysis, different crack initiations were observed in terms of ICF versus HCF regimes. Interestingly, for each life regime, similar failure mechanisms were observed for both surface conditions. Fig. 7 shows the final fracture surfaces with/without color contour maps to indicate the main failure mechanism of multiple specimens: (a) V02 (as-built surface in ICF regime), (b) V09 (half-polished surface in ICF regime), (c) V14 (as-built surface under in regime), and (d) V13 (half-polished surface in HCF regime). Regardless of the surface condition, the cracks are initiated from the surface. Relatively

Table 3
Strain-followed by force-controlled fatigue testing results of LB-PBF Ti-6Al-4V in as-built and half-polished surface conditions.

| Surface condition	Spec ID	Freq (Hz)	ε_{max} (mm/mm)	ε_{min} (mm/mm)	R_ε	σ_{max} (MPa)	σ_{min} (MPa)	R_σ	Reversals to failure ($2N_f$)
As-built	V02	5	0.0040	0.0004	0.1	479.4	48.9	0.10	91,718
	V10	5	0.0040	0.0004	0.1	489.5	56.7	0.12	98,354
	V16	7.5	0.0030	0.0003	0.1	357.6	35.6	0.10	220,026
	V04	7.5	0.0030	0.0003	0.1	376.4	49.0	0.13	182,444
	V08	7.5	0.0030	0.0003	0.1	356.5	39.1	0.11	272,928
	V18	8	0.0025	0.00025	0.1	283.2	28.3	0.10	518,256
	V12	8	0.0025	0.00025	0.1	310.8	36.3	0.12	384,808
	V14	8	0.0025	0.00025	0.1	307.2	31.2	0.10	641,712
	V06	10	0.0020	0.0002	0.1	243.2	32.4	0.13	>10,000,000
Half-polished	V07	5	0.0040	0.0004	0.1	496.6	57.9	0.12	101,832
	V09	5	0.0040	0.0004	0.1	490.5	61.5	0.13	121,984
	V15	7.5	0.0030	0.0003	0.1	359.8	37.2	0.10	265,336
	V05	7.5	0.0030	0.0003	0.1	378.9	50.0	0.13	307,080
	V03	7.5	0.0030	0.0003	0.1	361.0	41.6	0.12	326,246
	V13	8	0.0025	0.00025	0.1	303.9	30.7	0.10	574,122
	V11	8	0.0025	0.00025	0.1	307.2	34.3	0.11	582,412
	V17	8	0.0025	0.00025	0.1	300.4	32.6	0.11	791,602
	V01	10	0.0020	0.0002	0.1	248.1	24.8	0.10	>10,000,000
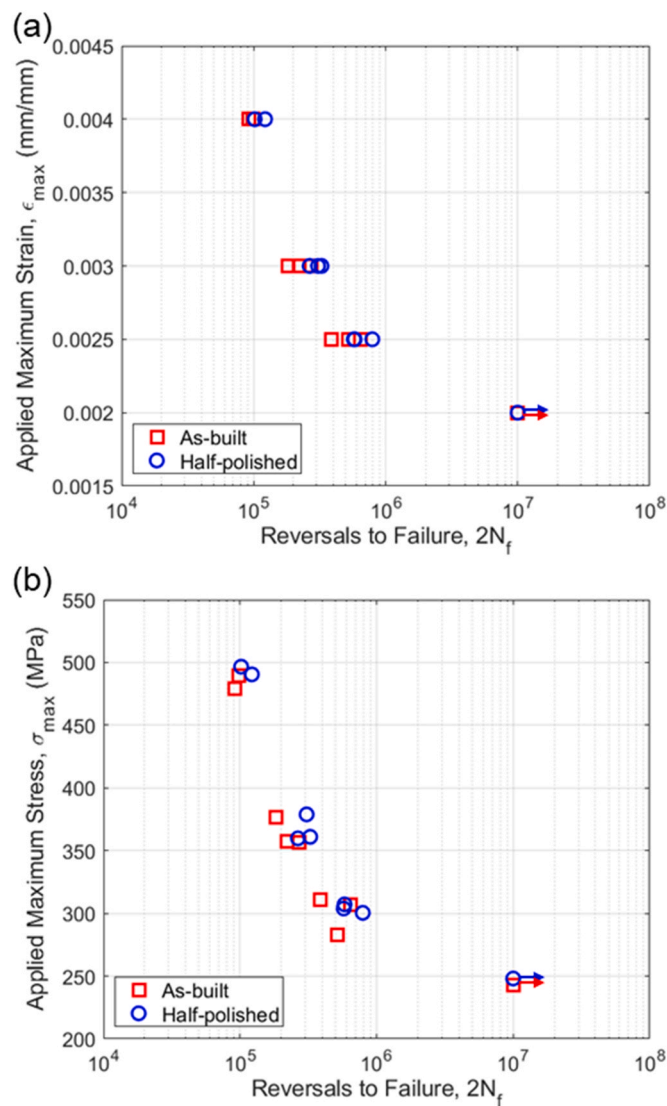
Fig. 6. (a) Strain-life and (b) stress-life plots of LB-PBF Ti-6Al-4V specimens with as-built and half-polished surface conditions.

more crack initiations on different planes and coalesces are observed in the ICF regime, while a primary crack initiation dominated the fatigue failure in the HCF regime. This can be explained by the relatively longer crack growth stage in the ICF regime allowing for other cracks to initiate [53,54]. As a result, fractography reveals that fatigue failure mechanisms can be similar for as-built and half-polished specimens, even though the specimens have very different values of conventional standard SR parameters.

4. Data analysis and parameter development

4.1. Data validation

It is important to ensure that imaging data is robust enough for the sake of analysis. Specifically, we need to know whether the resolution employed and the area scanned are sufficient to accurately represent the SR of the entire part and to obtain accurate estimates of standard (and new) SR parameters. Hence, data validation procedures were conducted. First, the resolution of the image was inspected, namely, whether 500X magnification could provide high enough accuracy regarding height data compared to higher magnifications. Fig. 8 shows bar plots of standard SR parameters measured at 500X and 1000X magnifications.

All the measurements in Fig. 8 are close to each other, regardless of magnifications, which means that for the sake of calculating standard SR parameters, using 1000X does not provide significantly different results than 500X. On the other hand, 1000X imaging takes four times more time and memory than 500X. As a result, the height data measured by processing microscopy images at 500X magnification in this study was considered sufficient and it was deemed a good compromise for image resolution versus time and storage efficiency.

The entire area of the gage section of the specimen could not be scanned due to the limitations of the Keyence VHX-6000 3D digital microscope; hence, the gage section was divided into two sub-areas and scanned. This required determining whether there was any difference between the standard SR parameters of the entire area and sub-areas or not. In case the parameters obtained from the sub-areas differed significantly, this implied having to take two scans for each part and somehow combine them after the fact. To examine these differences, statistical analysis regarding the effect of measuring each sub-area on resulting standard SR measurements was conducted. A simulation process was designed in which the original microscopy image was randomly divided into multiple sub-areas (25% area, 25% length, 25% width, 50% length, and 50% width). The multiple sub-areas are schematically described with different colors in Fig. 9(a). This process was applied to all specimens for which microscopy images were present. SR parameters of each sub-area were computed and compared with the parameters of the whole surface. The results are plotted in Fig. 9(b). In this image, each color denotes a sub-area category and the length of the bars are average measurements over all the parts. The length of the bars are 95% confidence intervals associated with each measurement.

As can be viewed in Fig. 9, 50% length measurements (colored orange in Fig. 9) yield similar values of R_a and R_q but provide lower values of R_v and R_z compare to original measurements. This is because either the maximum or minimum height value of the entire profile and part of the profile can be significantly different, while the average values will remain similar. However, the discrepancy in R_v and R_z was not observed between 50% width measurements (colored dark golden in Fig. 9) and original measurements. SR profile lines of AM parts need to be parallel to the build orientation based on the ISO standard [40]. The layer-by-layer process tends to produce surface undulations with a period on the order of the layer thickness. Therefore, 50% length measurements result in shorter horizontal profile lines, while 50% width measurements keep the same length of horizontal profile lines compared to the 100% length measurements. As a result, a longer sampling length will tend to give greater values of R_v and R_z compared to shorter lengths. This observation using a data-driven comparison between various sub-sectional areas confirmed that SR analysis for fatigue critical applications should be conducted with longer profiled lines as much as possible.

4.2. Surface roughness parameters modification

The effect of the polishing process on surface topography can be visualized as a histogram of the point height data from the surface profile. Fig. 10 describes the number of data points in terms of profiled surface height of specimen V17 before and after the polishing process. The modes, the most counted value in a set of height data, before and after polishing are ~2 μm and ~18 μm from the mean, described as dotted lines in Fig. 10, respectively. In addition, the shape of the histogram shows that the surface before polishing has normally distributed height data. On the other hand, the surface after polishing has a distribution with negative skewness and the data is more weighted (or centered) around both the mean and the mode compared to the as-built surface data, where the data has a wider distribution. This negative skewness demonstrates that the polishing step results in a higher frequency of data points along the newly generated surfaces created by removal of the peaks. A height distribution that is negatively skewed and heavily concentrated around the mode may be observed not only after polishing, but also other surface treatment methods such as shot-
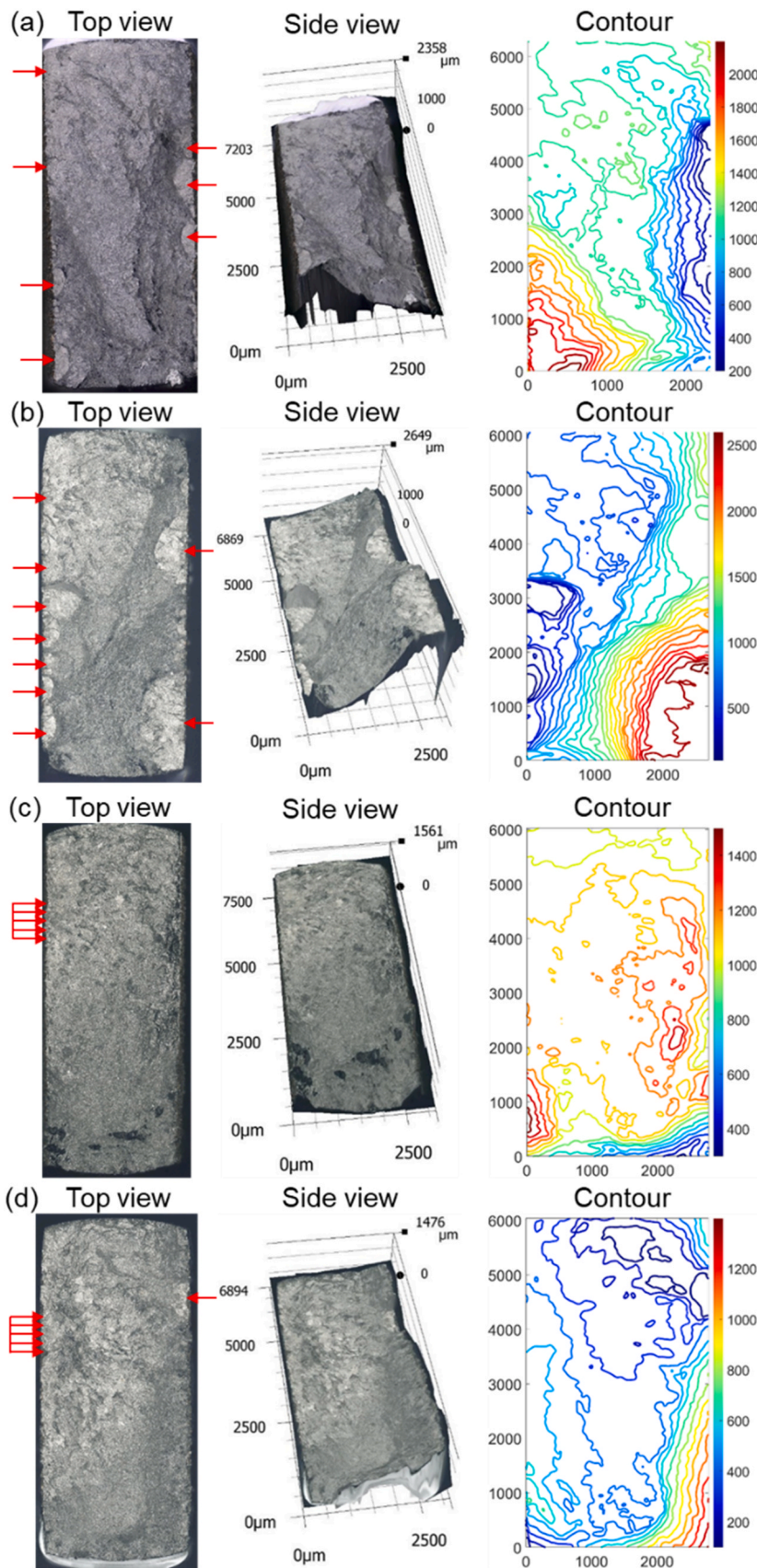
Fig. 7. Cross-sectional images of the final fractured surface of fatigue specimens including top/side view and colored contour line: (a) V02 (as-built, ε_{max} = 0.004 mm/mm (ICF)), (b) V09 (half-polished, ε_{max} = 0.004 mm/mm (ICF)), (c) V14 (as-built, ε_{max} = 0.0025 mm/mm (HCF)), and (d) V13 (half-polished, ε_{max} = 0.0025 mm/mm (HCF)). Arrows show the crack initiation sites for each specimen (For interpretation of the references to color in this figure legend, the reader is referred to the web version of this article).
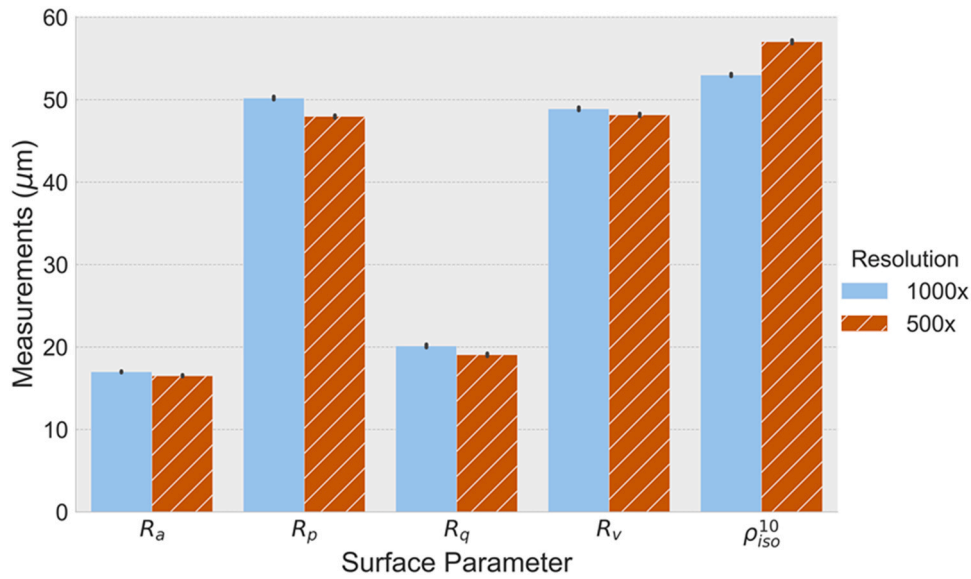
Fig. 8. The bar plots of several standard SR parameters based on the height data measured by 500X and 1000X magnifications.
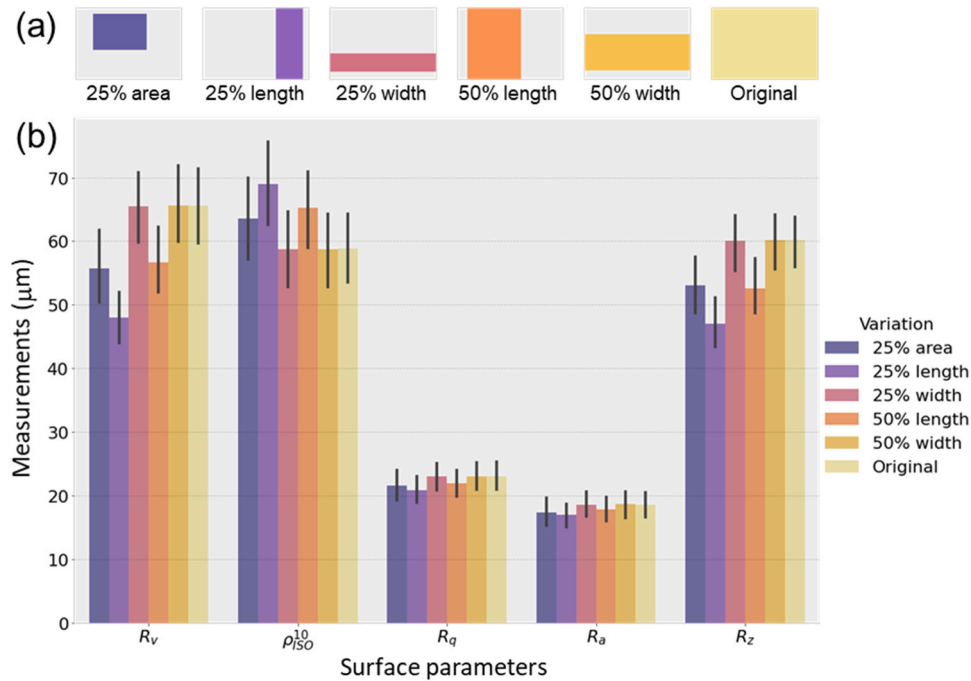

Fig. 9. (a) Schematically described sub-areas with various colors, and (b) standard SR parameters of each sub-areas with corresponded colors (For interpretation of the references to color in this figure legend, the reader is referred to the web version of this article).

peening and sand-blasting since these treatments will also physically smoothen the surface from the top, without much effect on valleys. As such, modified SR parameters that can distinguish these statistical characteristics regarding height data distributions are critical to advancing the use of AM parts that will be subjected to structural loads without sufficient removal of the as-built surfaces (e.g. internal features, complex or topology optimized structures).

The current standard SR parameters listed in ISO [40] are based on the distance from the mean of profiled height (e.g. R_v and S_v are the lowest height point from the mean line). These standard SR parameters can adequately characterize the surface with normally distributed height data (e.g. as-built specimens) as explained in the introduction. In order to examine the correlation between SR and fatigue life, the

standard SR parameters (R_v, and S_v) versus reversals to failures plot for both as-built and half-polished specimens at the applied maximum strain of $\varepsilon_{max} = 0.0025$ mm/mm are generated and shown in Fig. 11(a). A simple linear regression analysis using standard SR parameters as explanatory variables and reversals to failure as the response variable is conducted ($2N_f = \beta_0 + \beta_1 \times (R_v$ or $S_v)$). In addition, the coefficient of determination (R^2) for each corresponding regression line is calculated and provided in Fig. 11(a). Obtained R^2 values from different standard SR parameters are utilized to compare the strength of the linear relationship.

According to the R^2 values from Fig. 11(a), the one-dimensional parameter, R_v with $R^2 = 0.479$, exhibits less correlation with fatigue lives as compared to the two-dimensional parameters, S_v with R^2
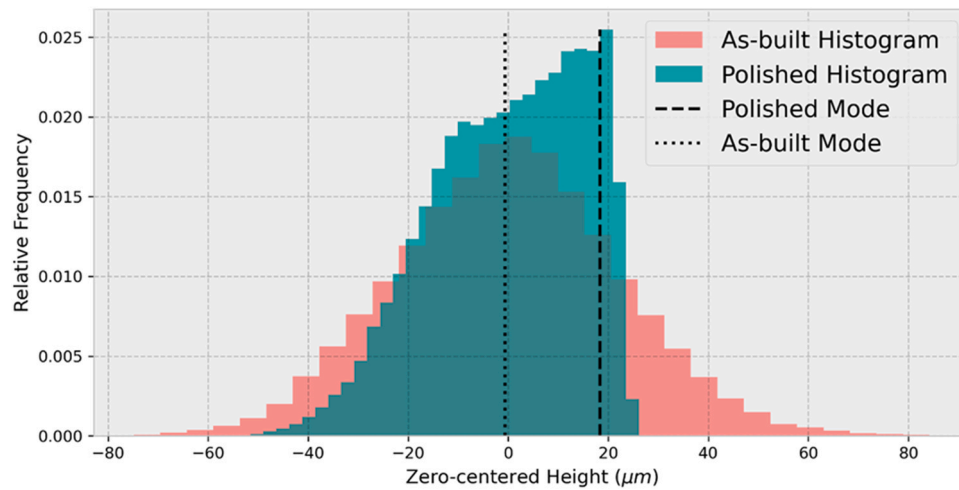
Fig. 10. The histogram of surface height data of specimen V17 before and after the polishing process. Both histograms are centered by the mean. The mode of each surface condition is indicated by different dotted lines.

$= 0.708$. This is because the profiled lines of one-dimensional parameter may miss deeper valleys among the entire surface, but the profiled areas of two dimensional parameter sample a greater region and are more capable of capturing the deepest valley on the surface. Gockel et al. [43] have also shown a similar observation using AM Inconel 718 alloy that S_v inversely correlates with the fatigue lives. Therefore, S_v shows better success than other standard SR parameters when correlating fatigue lives to SR.

When considering the S_v values of only as-built specimens to characterize fatigue lives, R^2 was 0.99. However, the presence of half-polished specimens provides invalid S_v values and results in less fitted trendlines of $R^2 = 0.708$, as shown in Fig. 11(a). Therefore, several modifications, mostly combining standard SR parameters regarding the valley of surface and distribution of height data, were conducted to adjust the correlation between SR and fatigue lives regardless of surface conditions. Fig. 11(b) includes two different hybrid area SR parameters that represent a reliable trend in terms of fatigue lives compared to other combined parameters. These two different hybrid area SR parameters are suggested based on the shifted baseline from the mean to the mode of the profiled surface. The first hybrid area SR parameter $S_v + S_{mode}$, the sum of the maximum valley depth of the profiled surface (S_v) and the distance between the mean and the most frequent value of the profiled surface (S_{mode}), describes the deepest valley of the profiled surface considering the height distribution. As a result of this correction, the R^2 between SR values to fatigue lives was increased from 0.708 (S_v) to 0.875 ($S_v + S_{mode}$), compare Fig. 11(a) and (b). This observation confirms that by shifting a baseline from the mean to the mode, more descriptive SR parameters regardless of the surface condition can be obtained.

Height direction characteristics such as the kurtosis of the profiled surface (S_{ku}) and the skewness of the profiled surface (S_{sk}) were also employed according to the literature to suggest better representative SR parameters in terms of fatigue lives [55–57]. Griffiths claimed that distribution and shape of surface topography can also influence fatigue behavior based on a survey about the relationship between the surface integrity and functionality [55,56]. Therefore, S_{mode} was multiplied by both S_{ku} and S_{sk} to obtain a hybrid area SR parameter which can yield a better correlation. The S_{sk} was multiplied by -1 because the negative skewness indicates the mass of the distribution is concentrated on the right side of the mean. The obtained hybrid area SR parameter, $S_v + S_{mode} \times S_{ku} \times S_{sk}$ shows considerable improvement with $R^2 = 0.978$ compared to $S_v + S_{mode}$ with $R^2 = 0.875$(see Fig. 11(b)).

The proposed hybrid area SR parameter results in an improved R^2 value for the combined dataset of as-built and half-polished surfaces. In addition, the $S_v + S_{mode}$ parameter shows a significantly improved correlation as compared to S_v since it considers the effect of height distribution. Moreover, the $Sv + S_{mode} \times S_{ku} \times S_{sk}$ parameter can represent the maximum valleys of the surface as a single parameter containing statistical remarks regarding the surface condition. As a result, the proposed $S_v + S_{mode} \times S_{ku} \times S_{sk}$ hybrid area SR parameter can be used as a concise and comprehensive SR parameter especially for the surface treated LB-PBF parts.

4.3. Effect of design and build orientation

The previous results suggest that the two-dimensional area SR parameters can provide more accurate description of the critical SR characteristics related to the fatigue failure as compared to parameters based on the line roughness. However, measuring area roughness is not always feasible because of the shape of fabricated parts (e.g. cylindrical shape specimens). Many of conventional SR analysis equipment provide correction functions which can adjust geometrical/dimensional effects on SR measurement. These shape/tilt correction methods center the data points on the average based on statistical analysis. However, it is always beneficial to avoid correction especially for the fatigue critical applications since the correcting process may result in some artificial errors. An alternative method of evaluating SR in real applications is utilizing the line roughness in the direction of loading. In this section, the SR data from a previous study [32] is employed to verify whether the proposed hybrid line SR parameter can successfully capture the differences in roughness among the various geometries and their associated effects on the fatigue performance.

The specimen design from the previous study was cylindrical dog-bone with uniform gage section and the build orientation was diagonal [32]. Hence, both geometrical effects from the cylindrical design and stair effects from the diagonal layer-by-layer fabrication process can be considered. Since the specimens were cylindrical and diagonally built, the critical roughness occurs as a line along the down-skin surface where the stair effects are most detrimental [58]. Therefore, the SR of five specimen batches with different dimensions were investigated by the 3D digital microscope using line profiles in [32]. Based on profiled line roughness data, standard (R_p, R_v, R_z, R_a, R_{sk}, R_{ku}, and R_{mode}) and suggested hybrid ($R_v + R_{mode}$ and $R_v + R_{mode} \times R_{ku} \times R_{sk}$) line SR parameters are calculated and listed in Table 4. Both down-skin and up-skin surfaces were measured; however, since all fatigue cracks were initiated from down-skin surface due to the relatively higher SR compare to the up-skin, only SR values of down-skin are listed in Table 4. It should be also noted that the values in Table 4 are average of 6 profiled
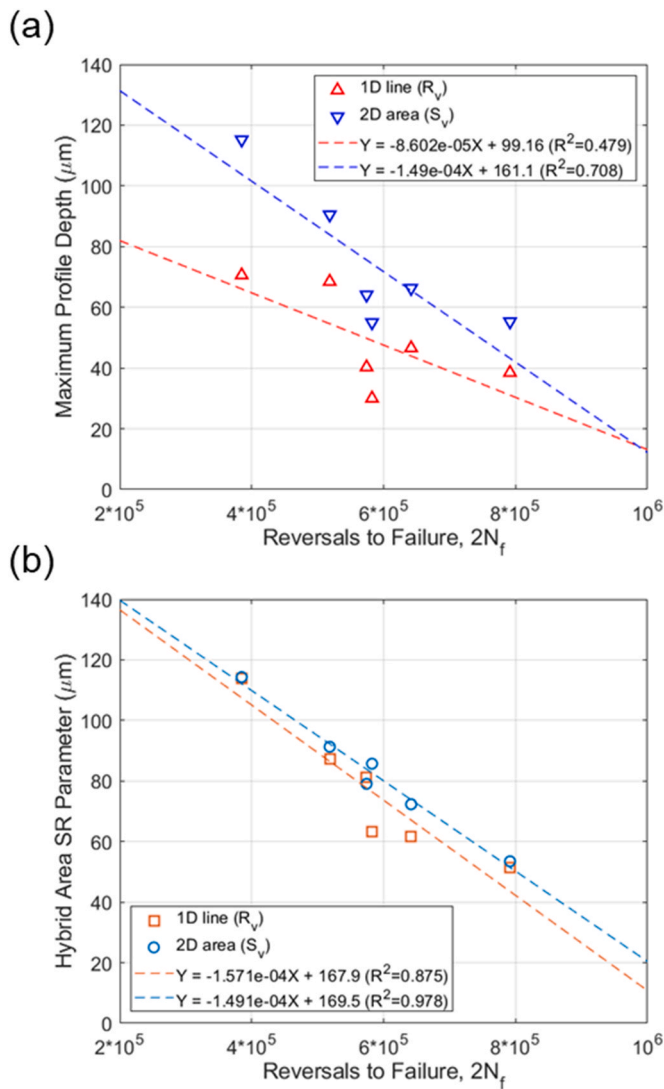
Fig. 11. SR values versus reversals to failure for specimens tested at ε_{max} = 0.0025 mm/mm are plotted regardless of surface conditions (both as-built and half-polished are included): (a) Existing standard SR parameters and (b) the proposed hybrid area SR parameters. Their trendlines and coefficient of determinations are also plotted and written, respectively.

line roughness measurements.

Fig. 12 shows the standard and hybrid line SR parameters versus fatigue lives similar to the Fig. 11(b) to validate the use of hybrid line SR parameters rather than hybrid area SR parameters. All data points in Fig. 12 were tested under ~200 MPa stress amplitude and include all five geometries from the previous study. The SR parameter needs to capture this trend since other conditions that affect fatigue strength are restricted and cracks were initiated from the surface. The standard and suggested hybrid line SR parameters (R_v and $R_v + R_{mode} \times R_{ku} \times R_{sk}$) were used to generate Fig. 12, yielding $R^2 = 0.693$ and $R^2 = 0.485$, respectively. It should be noted that the scatter observed for hybrid line

SR is much greater as compared to the hybrid area SR, which is related to the smaller sample size of line measurements compare to area measurements. Additionally, for these specimen geometries and build direction the location of the highest roughness region of the specimen is easily identifiable due to the down skin surface condition. Despite the small difference in the coefficient of determination, agreement between the standard and hybrid surface parameter for these surface conditions further demonstrates the usefulness of the hybrid parameter to adequately describe the surface condition.

It is demonstrated here that using the hybrid line SR parameter as a substitute for the hybrid area SR parameter is valid for geometries, such as cylindrical surfaces, where area measurements may introduce uncertainty/errors in the measured values. The hybrid line SR parameter, $R_v + R_{mode} \times R_{ku} \times R_{sk}$, appropriately captures the SR effects on fatigue life in the HCF regime, while standard SR parameters require additional efforts such as slope/tilt corrections. To investigate whether this parameter can replace the standard SR parameters in existing fatigue prediction models or not, further discussions are included in the following modeling section.

5. Fatigue modeling based on surface roughness

Neuber [44] has proposed a semiempirical relationship to rationalize the stress concentration factor using SR parameters, expressed by Eq. (3):

$$\overline{K}_t = 1 + n\sqrt{\lambda \frac{R_z}{\rho}} \tag{3}$$

where n is the stress state (i.e. n = 1 for shear and n = 2 for tension), λ is the ratio between spacing and height of surface irregularities, and ρ is the radius of notch on the surface. Based on this semiempirical
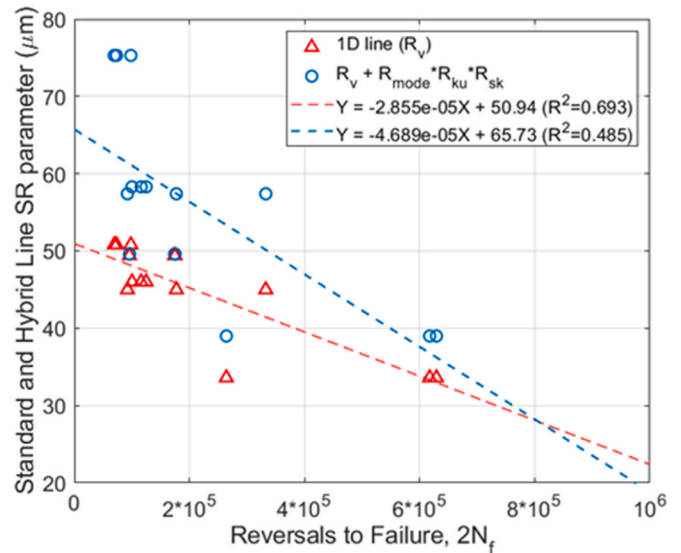

Fig. 12. The proposed hybrid line SR parameters ($R_v + R_{mode}$ and $R_v + R_{mode} \times R_{ku} \times R_{sk}$) versus reversals to failure for specimens tested at σ_a = ~200 MPa.

Table 4
Calculated standard and suggested hybrid line SR parameters based on the data from a previous study [32].

Geometry	R_p (μm)	R_v (μm)	R_z (μm)	R_a (μm)	R_{sk}	R_{ku}	R_{mode} (μm)	$R_v + R_{mode}$ (μm)	$R_v + R_{mode} \times R_{sk} \times R_{ku}$ (μm)
Batch 1	42.3	33.6	75.9	13.8	0.3	3.1	-0.7	33.0	39.0
Batch 2	48.4	45.0	93.4	20.3	0.2	2.4	9.3	54.3	57.4
Batch 3	71.7	49.4	121.1	20.3	0.6	3.5	-6.7	42.7	49.6
Batch 4	51.0	46.0	97.0	19.6	0.2	2.6	-3.7	42.4	58.3
Batch 5	64.9	50.8	115.7	22.1	0.4	2.9	-6.7	44.1	75.3

approach, Arola and Ramulu [59] proposed a model for fiber reinforced plastics. In this model, the effective elastic stress concentration factor ($\overline{K}_t$) is obtained by various SR parameters and radii of curvatures, expressed by Eq. (4):

$$\overline{K}_t = 1 + n\left(\frac{R_a}{\overline{\rho}_{10}}\right)\left(\frac{R_t}{R_{zISO}}\right) \tag{4}$$

where n is again the stress state, $\overline{\rho}_{10}$ is the effective radius of curvature taken from the dominant profiled valleys of the 10-point height roughness (R_{zISO}) and R_a and R_t are standard SR parameters. Therefore, valleys on the surface are considered as micro-notches and both depth and shape of micro-notches are utilized in this model. The calculated effective elastic stress concentration factor derives the effective fatigue notch factor ($\overline{K}_f$), which can be utilized as a knock-down factor for the fatigue endurance limit (σ_e), obtained from specimens with machined/polished surfaces. Eqs. (5) and (6) describe the notch sensitivity of the material (q) and the effective fatigue notch factor ($\overline{K}_f$):

$$q = \frac{1}{1 + \frac{\gamma}{\overline{\rho}_{10}}} \tag{5}$$

$$\overline{K}_f = 1 + q(\overline{K}_t - 1) \tag{6}$$

where γ is a material characteristic length.

The Arola-Ramulu model was used in previous studies [46,47] to predict fatigue lives of as-built LB-PBF 304LSS and Ti-6Al-4V specimens from the machined/polished ones. However, the equation of $\overline{K}_t$ to obtain the final notch factor are quite complicated due to the measurement of $\overline{\rho}_{10}$, which can introduce human induced measurement errors. Therefore, in this section, a simplified fatigue prediction model using the proposed data driven hybrid SR parameter to accommodate various surface conditions is explored. To adequately challenge the proposed hybrid SR parameter, the fatigue test results from the aforementioned previous studies, as-built round specimens fabricated diagonally from [32,60]. The different specimen geometries in [32] resulted in measurably different surface roughness and a shift in HCF performance. Even though the data originated from different studies, the specimens were fabricated by the same LB-PBF EOS M290 machine with the same process parameters.

The modified fatigue prediction model is based on using simplified variables to reduce the number of parameters with the goal to minimize user related measurement errors. Variables $\overline{K}_t$ and q to derive $\overline{K}_f$ are modified using the proposed hybrid SR parameter and the effective radius of curvature ($\overline{\rho}$). The fundamental mechanism of LB-PBF is a layer-by-layer melting process; thus, each layer tends to create new topographical features on the top of the previous layer. Since the pri-

mary roughness can be related to the layer thickness, it stands to reason that the critical micro-notches that lead to failure will be on the order of the layer thickness, approximately [61]. This is demonstrated in Fig. 13 where the diameter of the primary roughness is considered to be the layer thickness and therefore the effective radius ($\overline{\rho}$) is half the layer thickness. It should be noted that this is an oversimplification in estimating $\overline{\rho}_{10}$, but eliminates the subjective measurements of these radii, and thus, improves the repeatability of the predictions across different users. The depth of the effective notch can be approximately represented by the hybrid SR parameter as statistical effects due to post surface treatments are already considered in the hybrid SR parameter.

The proposed hybrid line SR parameter ($R_v + R_{mode} \times R_{ku} \times R_{sk}$) is employed instead of R_a, R_t, and R_{zISO} in the equation for $\overline{K}_t$ proposed by Arola-Ramulu (Eq. 4) since hybrid SR parameter can capture both statistical effects and concomitants due to post-process surface treatments without additional terms. As a result, the effective elastic stress concentration factor ($\overline{K}_t$) and the notch sensitivity of the material (q) have been modified as followed in Eqs. (7) and (8):

$$\overline{K}_t = 1 + n\left(\frac{R_a}{\overline{\rho}_{10}}\right)\left(\frac{R_t}{R_{zISO}}\right) = 1 + n\left(\frac{R_v + R_{mode} \times R_{ku} \times R_{sk}}{\overline{\rho}}\right) \tag{7}$$

$$q = 1 \Big/ \left(1 + \frac{\gamma}{\overline{\rho}}\right) \tag{8}$$

where the material characteristic length (γ) was 1.5 μm which is the average acicular α' grain width of the Ti-6Al-4V material [32]. The width of the α' grains generally represents the slip length of martensitic titanium alloys. Williams and Luetjering [62] showed that, for Ti-Al alloys of constant slip character, the fracture strain increases with the inverse of slip length, while the fracture stress increases with the inverse square root of the slip length. As such, the average grain size has been used to represent notch sensitivity [63] and is considered here as a measurable, rather than empirical, material characteristic length.

The proposed new fatigue model derived from modified $\overline{K}_t$ and q is validated with experimental data from previous studies: the fatigue test results of batch 1 and 3 are adopted from Pegues et al. [32] and machined/polished data is adopted from Carrion et al. [60]. Fig. 14 contains stress-life plots with referenced fatigue data points and estimated fatigue lives using the Arola-Ramulu model and the proposed approach in this study. For clarify, modified $\overline{K}_t$, q, and K_f are listed in Table 5. The fatigue test results of batch 1 and batch 3, which respectively represent least and most severe surface roughness of the five batches, are considered [46]. It should be noted that statistical analysis carried out in [32] suggests that the surface roughness among batches 2–5 were not significantly different, and thus, similarity in their fatigue lives were observed. Fig. 14(a) shows the fatigue prediction curves based
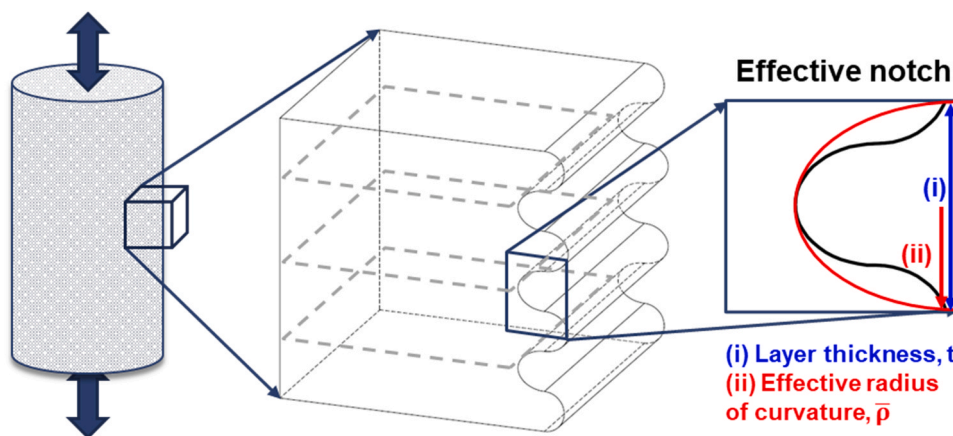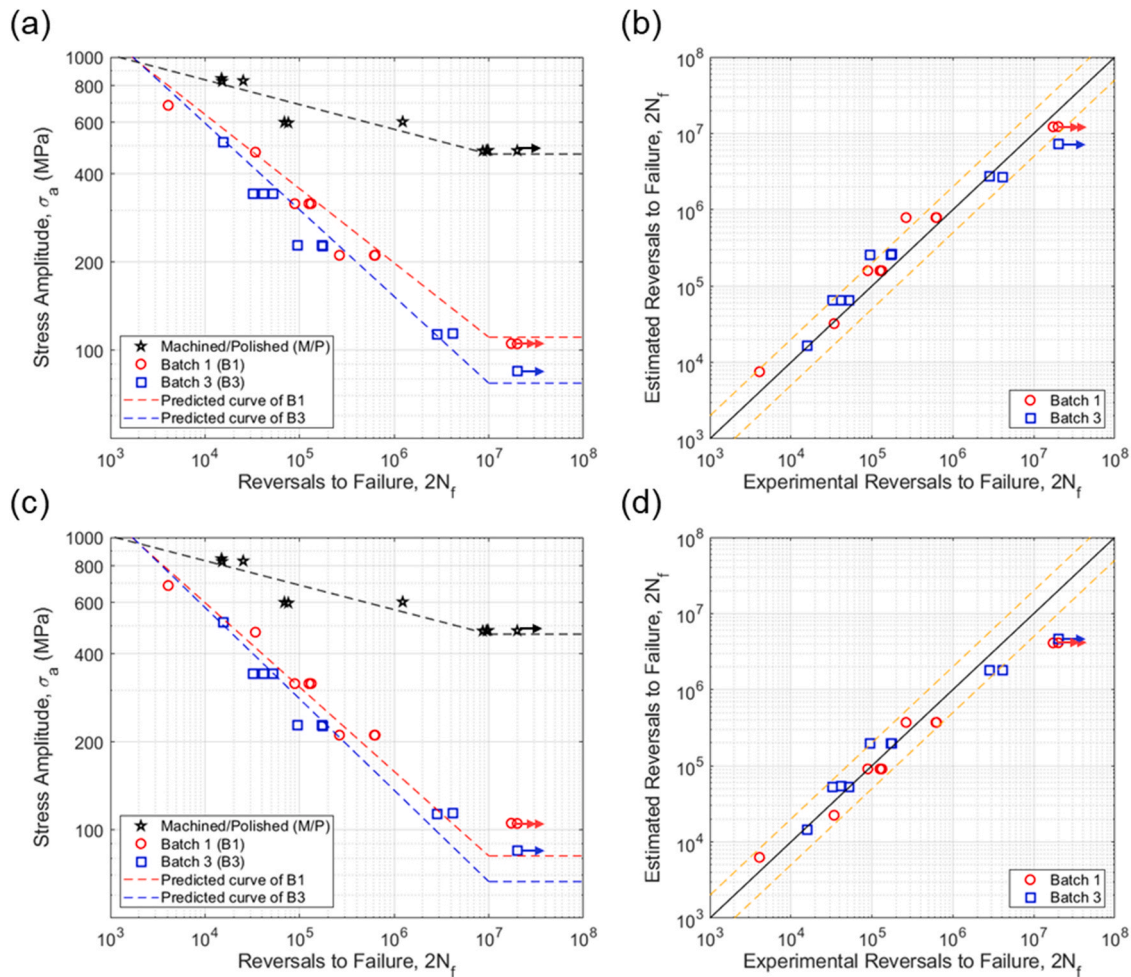

Fig. 13. Schematic image of the gage section of specimen and the enlarged as-built surface with indications of each layer. The highlighted area indicates effective notch which is determined by the hybrid SR parameter ($R_v + R_{mode} \times R_{ku} \times R_{sk}$) with indications of layer thickness (t), and effective radius of curvature ($\overline{\rho}$).

Fig. 14. (a) Fatigue prediction curves based on the Arola-Ramulu model, and (b) the estimated fatigue lives compare to empirical data with the scatter band of 2. (c) Fatigue prediction curves based on the modified $\overline{K}_f$ model and the proposed hybrid SR parameter, and (d) the estimated fatigue lives compare to empirical data with the scatter band of 2.

Table 5
Calculated modified $\overline{K}_t$, q, and $\overline{K}_f$ of batch 1 and 3.

# of Batch	$\overline{K}_t$	q	K_f
Batch 1	4.45	0.91	4.14
Batch 3	4.75	0.91	4.41

on the previously used Arola-Ramulu model (Eqs. 4–6) and Fig. 14(b) shows the estimated fatigue lives compare to experimental data. In addition, the fatigue prediction curves using the proposed fatigue model (Eqs. 6–8) are plotted in Fig. 14(c) and the estimated and experimented fatigue lives are indicated in Fig. 14(d).

Arola-Ramulu model slightly overestimated the fatigue lives in ICF regime; however, the estimated endurance limit at 10^7 cycles is within the scatter bands of 2. While the proposed model from Eqs. (7) and (8) better represents the failed tests, the predicted endurance limit at 10^7 cycles is lower than what was observed experimentally. This overestimation of the surface effect on fatigue strength in the HCF regime is most likely related to the increasing role of internal cleavage crack initiation, a well-known failure mechanism for low stress cyclic behavior of Ti-6Al-4V [64,65]. Considering the presence of volumetric defects associated with AM, the shift from surface to internal crack initiation would ultimately result in fatigue performance more closely related to the machined and polished condition requiring tens of millions of cycles to reach failure. To overcome the discrepancy between experimental

and estimated fatigue lives of LB-PBF Ti-6Al-4V specimens close to endurance limits, the tri-slope model can be adapted to better represent the HCF behavior of materials such as titanium alloys that do not have well defined endurance limits [24]. Testing into the VHCF regime would be a necessary approach to fully understand this transitional behavior for AM Ti alloys and is beyond the scope of the present work. An important observation, however, is the predictions with the new model are more conservative even in the high cycle regime which is an important consideration for design of fatigue critical components. From the perspective of designing components for fatigue critical applications, a model that conservatively estimates fatigue lives is often preferred. Therefore, the proposed fatigue model shows more conservative predictions as compared to the Arola-Ramulu model, especially for the failed tests in the HCF. The results confirmed that the hybrid line SR parameter ($R_v + R_{mode} \times R_{ku} \times R_{sk}$) and the simplified effective radius of curvature ($\overline{\rho}$) can be utilized as alternative variables to predict the fatigue performance of AM parts with SR. The data driven hybrid SR parameter is not sensitive to post-process surface treatments that alter the standard SR parameters without significantly impacting on the fatigue behavior.

6. Conclusions

The main objective of this study was to examine the correlation between surface roughness parameters and fatigue behavior of LB-PBF Ti-6Al-4V specimens using conventional universal measurement methods.

The surface roughness parameters were examined using data-driven surface topography analysis. From the performed experiments and analyses, the following concluding remarks can be made:

1. Fatigue lives of as-built and half-polished specimens were similar even though their standard surface roughness parameters (i.e. R_v and S_v) were significantly different due to their distinct height data distributions.
2. In order to accurately correlate surface roughness parameters and fatigue lives regardless of the surface condition, the values that represent height data distribution such as mode, skewness and kurtosis need to be considered together with the maximum valley depth value, $S_v + S_{mode} \times S_{ku} \times S_{sk}$.
3. Geometry must be considered to adequately determine the appropriate surface roughness measurement approach. While area measurements may be feasible for flat surfaces, and therefore, recommended, cylindrical surfaces may require line measurements along the loading direction. The hybrid line roughness parameters with the suggested formula (e.g. $R_v + R_{mode} \times R_{ku} \times R_{sk}$) can be used as an alternative parameter.
4. The modified fatigue modeling based on the proposed hybrid surface roughness parameter estimated the fatigue lives of LB-PBF Ti-6Al-4V specimens with different levels of surface roughness reasonably well with most of the data within the scatter bands of 2.

The proposed fatigue model not only demonstrated accurate predictive capability for failed test specimens but also reduced the number of variables that require additional efforts to measure. It should also be noted that this fatigue prediction model requires only standard tensile properties, the endurance limit of machined/polished specimens, layer thickness, and the proposed hybrid surface roughness parameter. The value of such predictive capabilities without requiring additional fatigue data is remarkable for AM materials which, depending on process and post-process conditions, can have considerable differences in surface roughness. This fatigue life prediction pathway, therefore, has great potential as a non-destructive approach for design engineers concerned with the fatigue behavior of AM parts with complex geometries or topological optimized features for which the surface roughness cannot be completely removed by post-processing.

CRediT authorship contribution statement

Seungjong Lee: Conceptualization, Methodology, Validation, Formal analysis, Investigation, Data curation, Writing - original draft, Visualization. **Behnam Rasoolian:** Conceptualization, Methodology, Software, Data curation, Validation, Investigation, Writing - original draft. **Daniel F. Silva:** Conceptualization, Methodology, Resources, Formal analysis, Investigation, Writing - review & editing, Supervision, Project administration. **Jonathan W. Pegues:** Validation, Formal analysis, Data curation, Writing - review & editing. **Nima Shamsaei:** Conceptualization, Methodology, Resources, Formal analysis, Investigation, Writing - review & editing, Supervision, Project administration, Funding acquisition.

Declaration of Competing Interest

The authors declare that they have no known competing financial interests or personal relationships that could have appeared to influence the work reported in this paper.

Acknowledgments

References

[1] T. DebRoy, H.L. Wei, J.S. Zuback, T. Mukherjee, J.W. Elmer, J.O. Milewski, A. M. Beese, A. Wilson-Heid, A. De, W. Zhang, Additive manufacturing of metallic components – process, structure and properties, Prog. Mater. Sci. 92 (2018) 112–224, https://doi.org/10.1016/j.pmatsci.2017.10.001.

[2] D.D. Gu, W. Meiners, K. Wissenbach, R. Poprawe, Laser additive manufacturing of metallic components: materials, processes and mechanisms, Int. Mater. Rev. 57 (2012) 133–164, https://doi.org/10.1179/1743280411Y.0000000014.

[3] W.E. Frazier, Metal additive manufacturing: a review, J. Mater. Eng. Perform. 23 (2014) 1917–1928, https://doi.org/10.1007/s11665-014-0958-z.

[4] D. Herzog, V. Seyda, E. Wycisk, C. Emmelmann, Additive manufacturing of metals, Acta Mater. 117 (2016) 371–392, https://doi.org/10.1016/j.actamat.2016.07.019.

[5] S.L. Sing, J. An, W.Y. Yeong, F.E. Wiria, Laser and electron-beam powder-bed additive manufacturing of metallic implants: a review on processes, materials and designs, J. Orthop. Res. 34 (2016) 369–385, https://doi.org/10.1002/jor.23075.

[6] N. Shamsaei, A. Yadollahi, L. Bian, S.M. Thompson, An overview of direct laser deposition for additive manufacturing; Part II: mechanical behavior, process parameter optimization and control, Addit. Manuf. 8 (2015) 12–35, https://doi.org/10.1016/j.addma.2015.07.002.

[7] J.J. Lewandowski, M. Seifi, Metal additive manufacturing: a review of mechanical properties, Annu. Rev. Mater. Res. 46 (2016) 151–186, https://doi.org/10.1146/annurev-matsci-070115-032024.

[8] W.J. Sames, F.A. List, S. Pannala, R.R. Dehoff, S.S. Babu, The metallurgy and processing science of metal additive manufacturing, Int. Mater. Rev. 61 (2016) 315–360, https://doi.org/10.1080/09506608.2015.1116649.

[9] Y. Kok, X.P. Tan, P. Wang, M.L.S. Nai, N.H. Loh, E. Liu, S.B. Tor, Anisotropy and heterogeneity of microstructure and mechanical properties in metal additive manufacturing: a critical review, Mater. Des. 139 (2018) 565–586, https://doi.org/10.1016/j.matdes.2017.11.021.

[10] A. Yadollahi, N. Shamsaei, Additive manufacturing of fatigue resistant materials: challenges and opportunities, Int. J. Fatigue 98 (2017) 14–31, https://doi.org/10.1016/j.ijfatigue.2017.01.001.

[11] C.N. Elias, J.H.C. Lima, R. Valiev, M.A. Meyers, Biomedical applications of titanium and its alloys, JOM 60 (2008) 46–49, https://doi.org/10.1007/s11837-008-0031-1.

[12] G. Lutjering, J.C. Williams, Titanium, second ed., 2007. https://doi.org/10.1007/978-3-540-73036-1.

[13] I. Gurrappa, Characterization of titanium alloy Ti-6Al-4V for chemical, marine and industrial applications, Mater. Charact. 51 (2003) 131–139, https://doi.org/10.1016/j.matchar.2003.10.006.

[14] S. Gorsse, C. Hutchinson, M. Gouné, R. Banerjee, Additive manufacturing of metals: a brief review of the characteristic microstructures and properties of steels, Ti-6Al-4V and high-entropy alloys, Sci. Technol. Adv. Mater. 18 (2017) 584–610, https://doi.org/10.1080/14686996.2017.1361305.

[15] W.S.W. Harun, N.S. Manam, M.S.I.N. Kamariah, S. Sharif, A.H. Zulkifly, I. Ahmad, H. Miura, A review of powdered additive manufacturing techniques for Ti-6Al-4V biomedical applications, Powder Technol. (2018), https://doi.org/10.1016/j.powtec.2018.03.010.

[16] L.C. Zhang, Y. Liu, S. Li, Y. Hao, Additive manufacturing of titanium alloys by electron beam melting: a review, Adv. Eng. Mater. (2018), https://doi.org/10.1002/adem.201700842.

[17] H. Gong, K. Rafi, H. Gu, T. Starr, B. Stucker, Analysis of defect generation in Ti-6Al-4V parts made using powder bed fusion additive manufacturing processes, Addit. Manuf. 1 (2014) 87–98, https://doi.org/10.1016/j.addma.2014.08.002.

[18] A.M. Beese, B.E. Carroll, Review of mechanical properties of Ti-6Al-4V made by laser-based additive manufacturing using powder feedstock, JOM 68 (2016) 724–734, https://doi.org/10.1007/s11837-015-1759-z.

[19] A. Fatemi, R. Molaei, J. Simsiriwong, N. Sanaei, J. Pegues, B. Torries, N. Phan, N. Shamsaei, Fatigue behaviour of additive manufactured materials: an overview of some recent experimental studies on Ti-6Al-4V considering various processing and loading direction effects, Fatigue Fract. Eng. Mater. Struct. 42 (2019) 991–1009, https://doi.org/10.1111/ffe.13000.

[20] B.E. Carroll, T.A. Palmer, A.M. Beese, Anisotropic tensile behavior of Ti-6Al-4V components fabricated with directed energy deposition additive manufacturing, Acta Mater. 87 (2015) 309–320, https://doi.org/10.1016/j.actamat.2014.12.054.

[21] T. Voisin, N.P. Calta, S.A. Khairallah, J.B. Forien, L. Balogh, R.W. Cunningham, A. D. Rollett, Y.M. Wang, Defects-dictated tensile properties of selective laser melted Ti-6Al-4V, Mater. Des. 158 (2018) 113–126, https://doi.org/10.1016/j.matdes.2018.08.004.

[22] R. Molaei, A. Fatemi, N. Sanaei, J. Pegues, N. Shamsaei, S. Shao, P. Li, D.H. Warner, N. Phan, Fatigue of additive manufactured Ti-6Al-4V, Part II: the relationship between microstructure, material cyclic properties, and component performance, Int. J. Fatigue 132 (2020), 105363, https://doi.org/10.1016/j.ijfatigue.2019.105363.

[23] J.W. Pegues, S. Shao, N. Shamsaei, N. Sanaei, A. Fatemi, D.H. Warner, P. Li, N. Phan, Fatigue of additive manufactured Ti-6Al-4V, Part I: the effects of powder feedstock, manufacturing, and post-process conditions on the resulting microstructure and defects, Int. J. Fatigue 132 (2020), 105358, https://doi.org/10.1016/j.ijfatigue.2019.105358.

[24] R.I. Stephens, A. Fatemi, R.R. Stephens, H.O. Fuchs, Metal Fatigue in Engineering, second ed., John Wiley & Sons, 2000.

[25] T. Vilaro, C. Colin, J.D. Bartout, As-fabricated and heat-treated microstructures of the Ti-6Al-4V alloy processed by selective laser melting, Met. Mat. Trans. A 42 (2011) 3190–3199, https://doi.org/10.1007/s11661-011-0731-y.

[26] R. Molaei, A. Fatemi, N. Phan, Significance of hot isostatic pressing (HIP) on multiaxial deformation and fatigue behaviors of additive manufactured Ti-6Al-4V including build orientation and surface roughness effects, Int. J. Fatigue 117 (2018) 352–370, https://doi.org/10.1016/j.ijfatigue.2018.07.035.

[27] P.D. Nezhadfar, R. Shrestha, N. Phan, N. Shamsaei, Fatigue behavior of additively manufactured 17-4 PHstainless steel: Synergistic effects of surface roughness and heat treatment, Int. J. Fatigue 124 (2019) 188–204, https://doi.org/10.1016/j.ijfatigue.2019.02.039.

[28] A. Townsend, N. Senin, L. Blunt, R.K. Leach, J.S. Taylor, Surface texture metrology for metal additive manufacturing: a review, Precis. Eng. 46 (2016) 34–47, https://doi.org/10.1016/j.precisioneng.2016.06.001.

[29] E. Wycisk, A. Solbach, S. Siddique, D. Herzog, F. Walther, C. Emmelmann, Effects of defects in laser additive manufactured Ti-6Al-4V on fatigue properties, Phys. Procedia 56 (2014) 371–378, https://doi.org/10.1016/j.phpro.2014.08.120.

[30] D. Greitemeier, C. Dalle Donne, F. Syassen, J. Eufinger, T. Melz, Effect of surface roughness on fatigue performance of additive manufactured Ti–6Al–4V, Mater. Sci. Technol. 32 (2016) 629–634, https://doi.org/10.1179/1743284715Y.0000000053.

[31] P. Edwards, M. Ramulu, Fatigue performance evaluation of selective laser melted Ti-6Al-4V, Mater. Sci. Eng. A 598 (2014) 327–337, https://doi.org/10.1016/j.msea.2014.01.041.

[32] J. Pegues, M. Roach, R. Scott Williamson, N. Shamsaei, Surface roughness effects on the fatigue strength of additively manufactured Ti-6Al-4V, Int. J. Fatigue 116 (2018) 543–552, https://doi.org/10.1016/j.ijfatigue.2018.07.013.

[33] R. Shrestha, J. Simsiriwong, N. Shamsaei, Fatigue behavior of additive manufactured 316L stainless steel parts: Effects of layer orientation and surface roughness, Addit. Manuf. (2019), https://doi.org/10.1016/j.addma.2019.04.011.

[34] N.N. Kumbhar, A.V. Mulay, Post processing methods used to improve surface finish of products which are manufactured by additive manufacturing technologies: a review, J. Inst. Eng. India Ser. C. 99 (2018) 481–487, https://doi.org/10.1007/s40032-016-0340-z.

[35] L. Hackel, J.R. Rankin, A. Rubenchik, W.E. King, M. Matthews, Laser peening: a tool for additive manufacturing post-processing, Addit. Manuf. (2018), https://doi.org/10.1016/j.addma.2018.09.013.

[36] S. Lee, Z. Ahmadi, J.W. Pegues, M. Mahjouri-Samani, N. Shamsaei, Laser polishing for improving fatigue performance of additive manufactured Ti-6Al-4V parts, Opt. Laser Technol. 134 (2021), 106639, https://doi.org/10.1016/j.optlastec.2020.106639.

[37] M. Kahlin, H. Ansell, D. Basu, A. Kerwin, L. Newton, J.J. Moverare, Improved fatigue strength of additively manufactured Ti6Al4V by surface post processing, Int. J. Fatigue 134 (2020), 105497, https://doi.org/10.1016/j.ijfatigue.2020.105497.

[38] E. Maleki, S. Bagherifard, M. Bandini, M. Guagliano, Surface post-treatments for metal additive manufacturing: progress, challenges, and opportunities, Addit. Manuf. (2020), 101619, https://doi.org/10.1016/j.addma.2020.101619.

[39] A. du Plessis, P. Sperling, A. Beerlink, O. Kruger, L. Tshabalala, S.G. le Roux, Standard method for microCT-based additive manufacturing quality control 3: surface roughness, MethodsX 5 (2018) 1111–1116, https://doi.org/10.1016/j.mex.2018.09.004.

[40] International Organization for Standardization, ISO 4287:1997. Geometrical product specifications (GPS). Surface texture: profile method. Terms, definitions and surface texture parameters, Geneva, 1997.

[41] E. Kiliçkap, O. Çakir, M. Aksoy, A. Inan, Study of tool wear and surface roughness in machining of homogenised SiC-p reinforced aluminium metal matrix composite, J. Mater. Process. Technol. 164–165 (2005) 862–867, https://doi.org/10.1016/j.jmatprotec.2005.02.109.

[42] J.C. Fox, S.P. Moylan, B.M. Lane, Effect of process parameters on the surface roughness of overhanging structures in laser powder bed fusion additive manufacturing, Procedia CIRP 45 (2016) 131–134, https://doi.org/10.1016/j.procir.2016.02.347.

[43] J. Gockel, L. Sheridan, B. Koerper, B. Whip, The influence of additive manufacturing processing parameters on surface roughness and fatigue life, Int. J. Fatigue 124 (2019) 380–388, https://doi.org/10.1016/j.ijfatigue.2019.03.025.

[44] H. Neuber, Theory of notch stresses: principles for exact calculation of strength with reference to structural form and material, 1958.

[45] D. Arola, C.L. Williams, Estimating the fatigue stress concentration factor of machined surfaces, Int. J. Fatigue 24 (2002) 923–930, https://doi.org/10.1016/S0142-1123(02)00012-9.

[46] J.W. Pegues, N. Shamsaei, M.D. Roach, R.S. Williamson, Fatigue life estimation of additive manufactured parts in the as-built surface condition, Mat. Des. Process. Comm. 1 (2019), e36, https://doi.org/10.1002/mdp2.36.

[47] S. Lee, J. Pegues, N. Shamsaei, Fatigue behavior and modeling for additive manufactured 304l stainless steel: the effect of surface roughness, Int. J. Fatigue 141 (2020), 105856, https://doi.org/10.1016/j.ijfatigue.2020.105856.

[48] ASTM International, ASTM E466 Standard Practice for Conducting Force Controlled Constant Amplitude Axial Fatigue Tests of Metallic Materials, West Conshohocken, PA, 2002, pp. 1–6. https://doi.org/10.1520/E0466-07.2.

[49] ASTM International, Standard specification for additive manufacturing titanium-6 aluminum-4 vanadium with powder bed fusion, ASTM International, 2012, pp. 1–8. https://doi.org/10.1520/F2924-14.2.

[50] A. Fatemi, R. Molaei, S. Sharifimehr, N. Shamsaei, N. Phan, Torsional fatigue behavior of wrought and additive manufactured Ti-6Al-4V by powder bed fusion including surface finish effect, Int. J. Fatigue 99 (2017) 187–201, https://doi.org/10.1016/j.ijfatigue.2017.03.002.

[51] ASTM International, ASTM E606 Standard Test Method for Strain-Controlled Fatigue Testing, West Conshohocken, PA, 2008, pp. 1–16. https://doi.org/10.1520/mnl10913m.

[52] M. Hamidi Nasab, S. Romano, D. Gastaldi, S. Beretta, M. Vedani, Combined effect of surface anomalies and volumetric defects on fatigue assessment of AlSi7Mg fabricated via laser powder bed fusion, Addit. Manuf. (2019), 100918, https://doi.org/10.1016/j.addma.2019.100918.

[53] N. Shamsaei, A. Fatemi, Small fatigue crack growth under multiaxial stresses, Int. J. Fatigue 58 (2014) 126–135, https://doi.org/10.1016/j.ijfatigue.2013.02.002.

[54] N. Shamsaei, Multiaxial Fatigue and Deformation Including Non-Proportional Hardening and Variable Amplitude Loading Effects, Univeristy of Toledo, 2010.

[55] D. Novovic, R.C. Dewes, D.K. Aspinwall, W. Voice, P. Bowen, The effect of machined topography and integrity on fatigue life, Int. J. Mach. Tools Manuf. 44 (2004) 125–134, https://doi.org/10.1016/j.ijmachtools.2003.10.018.

[56] B. Griffiths, Manufacturing Surface Technology: Surface Integrity and Functional Performance, Elsevier, 2001.

[57] K. Stout, L. Blunt, Three Dimensional Surface Topography, Elsevier, 2000.

[58] G. Strano, L. Hao, R.M. Everson, K.E. Evans, Surface roughness analysis, modelling and prediction in selective laser melting, J. Mater. Process. Technol. 213 (2013) 589–597, https://doi.org/10.1016/j.jmatprotec.2012.11.011.

[59] D. Arola, M. Ramulu, An examination of the effects from surface texture on the strength of fiber reinforced plastics, J. Compos. Mater. 33 (1999) 102–123, https://doi.org/10.1177/002199839903300201.

[60] P.E. Carrion, A. Soltani-Tehrani, N. Phan, N. Shamsaei, Powder recycling effects on the tensile and fatigue behavior of additively manufactured Ti-6Al-4V parts, Jom 71 (2019) 963–973, https://doi.org/10.1007/s11837-018-3248-7.

[61] F. Calignano, Investigation of the accuracy and roughness in the laser powder bed fusion process, Virtual Phys. Prototyp. 13 (2018) 97–104, https://doi.org/10.1080/17452759.2018.1426368.

[62] J.C. Williams, G. Luetjering, The effect of slip length and slip character on the properties of titanium alloys, Titan 80 (1980) 671–681.

[63] R.W. Karry, T.J. Dolan, Influence of grain size on fatigue notch-sensitivity, University of Illinois at Urbana, Engineering Experiment Station, 1953.

[64] J. Ruppen, P. Bhowal, D. Eylon, A.J. McEvily, On the process of subsurface fatigue crack initiation in Ti-6Al-4V. ASTM Special Technical Publication, 1979. https://doi.org/10.1520/stp35884s.

[65] D.F. Neal, P.A. Blenkinsop, Internal fatigue origins in α-β titanium allols, Acta Met. 24 (1976) 59–63, https://doi.org/10.1016/0001-6160(76)90147-4.